

# Deciphering the solar coronal heating: Energizing small-scale loops through surface convection

D. NÓBREGA-SIVERIO <sup>1,2,3,4</sup>, F. MORENO-INSERTIS<sup>1,2</sup>, K. GALSGAARD <sup>5</sup>, K. KRIKOVA <sup>3,4</sup>, L. ROUPPE VAN DER VOORT <sup>3,4</sup>,  
R. JOSHI <sup>3,4</sup> AND M. S. MADJARSKA <sup>6,7</sup>

<sup>1</sup>*Instituto de Astrofísica de Canarias, E-38205 La Laguna, Tenerife, Spain*

<sup>2</sup>*Universidad de La Laguna, Dept. Astrofísica, E-38206 La Laguna, Tenerife, Spain*

<sup>3</sup>*Roseland Centre for Solar Physics, University of Oslo, PO Box 1029 Blindern, 0315 Oslo, Norway*

<sup>4</sup>*Institute of Theoretical Astrophysics, University of Oslo, PO Box 1029 Blindern, 0315 Oslo, Norway*

<sup>5</sup>*School of Mathematics and Statistics, University of St Andrews, St Andrews KY16 9SS, Scotland, UK*

<sup>6</sup>*Max Planck Institute for Solar System Research, Justus-von-Liebig-Weg 3, 37077 Göttingen, Germany*

<sup>7</sup>*Space Research and Technology Institute, Bulgarian Academy of Sciences, Acad. Georgy Bonchev Str., Bl. 1, 1113, Sofia, Bulgaria*

(Received October 23, 2023; Accepted November 17, 2023)

## ABSTRACT

The solar atmosphere is filled with clusters of hot small-scale loops commonly known as Coronal Bright Points (CBPs). These ubiquitous structures stand out in the Sun by their strong X-ray and/or extreme-ultraviolet (EUV) emission for hours to days, which makes them a crucial piece when solving the solar coronal heating puzzle. In addition, they can be the source of coronal jets and small-scale filament eruptions. Here we present a novel 3D numerical model using the Bifrost code that explains the sustained CBP heating for several hours. We find that stochastic photospheric convective motions alone significantly stress the CBP magnetic field topology, leading to important Joule and viscous heating concentrated around the CBP's inner spine at a few megameters above the solar surface. We also detect continuous upflows with faint EUV signal resembling observational dark coronal jets and small-scale eruptions when H $\alpha$  fibrils interact with the reconnection site. We validate our model by comparing simultaneous CBP observations from SDO and SST with observable diagnostics calculated from the numerical results for EUV wavelengths as well as for the H $\alpha$  line using the Multi3D synthesis code. Additionally, we provide synthetic observables to be compared with Hinode, Solar Orbiter, and IRIS. Our results constitute a step forward in the understanding of the many different facets of the solar coronal heating problem.

*Keywords:* magnetohydrodynamics (MHD) — methods: numerical — methods: observational — Sun: atmosphere — Sun: chromosphere — Sun: corona

## 1. INTRODUCTION

Understanding why the solar corona temperature is a few hundred times larger than that at the surface requires studying the heating mechanisms across different solar regions and phenomena (e.g., Parker 1972; Galsgaard & Nordlund 1996; Gudiksen & Nordlund 2005; Klimchuk 2006; Parnell & De Moortel 2012). A particularly important case is that of the Coronal Bright Points or CBPs, structures with projected sizes between 5 and 40 Mm that stand out with enhanced EUV and X-ray emission against the quiet Sun (Golub et al. 1974; Madjarska 2019). CBPs are often observed to appear above photospheric regions with a strong parasitic polarity

surrounded by a network predominantly of the opposite polarity, a situation that typically leads to a fan-spine magnetic structure with a nullpoint at several megameters in the corona (Zhang et al. 2012; Mou et al. 2016; Galsgaard et al. 2017; Madjarska et al. 2021; Cheng et al. 2023). Their relevance stems from their copious energy emission, representing the main contributor to high-energy radiation over the solar disk outside active regions (Mondal et al. 2023); as well as their nearly uniform presence in the Sun and their long lifetime, from hours to days (Madjarska 2019). Considered to be downscaled versions of active regions (Madjarska 2019; Gao et al. 2022), CBPs are composed of small-scale loops, making them a relevant case study for this kind of fundamental magnetic field topology (Rappazzo et al. 2008; Reale 2014). Moreover, CBPs can be the source regions of eruptions of both hot and cool plasma (Hong et al. 2014; Sterling et al.

2015; Kumar et al. 2019; Madjarska et al. 2022), which may constitute a significant input of energy and mass for the solar corona (Lionello et al. 2016; Viall & Borovsky 2020).

A significant theoretical effort has been devoted to studying the heating of CBPs through (a) analytical studies collectively known as Converging Flux Models (Priest et al. 1994; Dreher et al. 1997; Priest et al. 2018); (b) one-dimensional models of individual magnetic loops (Reale 2014); or (c) by means of multi-dimensional purely magnetohydrodynamical (MHD) models, mainly analyzing the energy conversion during magnetic reconnection (Galsgaard et al. 2000; von Rekowski et al. 2006; Santos & Büchner 2007; Javadi et al. 2011; Wyper et al. 2018; Syntelis et al. 2019). A drawback of these approaches is that they rely on ad-hoc driving mechanisms, imposing converging flows or large-scale surface motions in order to drive magnetic reconnection at the coronal nullpoint and get a CBP. These mechanisms do not reflect the actual stochastic convective flows in the solar photosphere, which have been shown to provide enough energy to heat the corona in previous numerical simulations (e.g., Gudiksen & Nordlund 2005; Rempel 2017; Chen et al. 2022). However, as we propose in this paper, the energy injection through surface convection may indeed be the source of the CBP heating. An additional drawback of previous CBP models is that they did not include an appropriate radiation treatment, thus ignoring important entropy sources in the lower atmosphere. This not only precludes the calculation of many basic observational diagnostics but also restricts the possibility of understanding the heating and cooling processes in the chromosphere.

In this Letter, we present a comprehensive 3D radiative-MHD model of a CBP based on a magnetic nullpoint configuration. Our model shows that a CBP can be powered for at least several hours through the continuous action of the underlying surface convection. The inclusion of the relevant radiation and entropy sources in our model allows us to analyze the associated deposition of energy in different layers of the solar atmosphere and the corresponding changes in the dynamics, including the study of hot ejections and small-scale eruptive chromospheric phenomena within the CBP. To validate our theoretical model, we also present simultaneous observations of a representative CBP from space (SDO) and from the ground (SST). Through forward modeling, we successfully reproduce the main observed features from SDO and SST, confirming the adequacy of our model across different atmospheric layers.

## 2. RESULTS

### 2.1. Overview of the Experiment

The initial configuration consists of a rotationally-symmetric 3D null point magnetic topology (see Figure A1 in Appendix A, where details concerning the initial condition and the numerical code are also given). The inner spine of the structure is rooted in a region with a parasitic positive polarity, while the fan structure is anchored in the surrounding field of the opposite sign. A general outlook of the subsequent evolution of the experiment can be gained through

Figure 1 and its associated animation. The initial topology structure is rapidly disrupted by the stochastic granulation in the photosphere leading to a magnetic network pattern of the predominant polarity at the surface; the overall magnetic field topology above is stressed and magnetic reconnection is triggered at the nullpoint. Simultaneously, the magnetic loops underneath the fan surface experience intense heating, giving rise to a CBP with conspicuously enhanced emissivity in EUV, X-rays, and UV, as evidenced in Figure 1 through the synthetic observables of panels (f), (g), (h), and (i) (see Appendix C for the calculation details). The diameter of the CBP, estimated from the EUV response at its base, is approximately 20 Mm, which is within the typical range reported in observations (5–40 Mm, see Madjarska 2019, and references therein).

The CBP nullpoint undergoes continuous perturbations, as illustrated in panel (b) through the time-evolution of its coordinates  $(x_{np}, y_{np}, z_{np})$ , which can be shifted by up to a few Mm, similarly to the nullpoint displacements inferred from observations (Galsgaard et al. 2017). Around  $t = 111.67$  min, the time of the snapshots in Figure 1, the current sheet around the nullpoint experiences a major disturbance, concerning both its location and shape. The reason for this perturbation is the approach of an elongated cool and dense structure to the reconnection site visible in panels (c) and (d). This structure is shown to be an  $H\alpha$  chromospheric fibril in Section 2.3. Throughout the evolution of the CBP, other chromospheric fibrils and spicule-like structures are found to develop in the lower atmosphere (see animation at  $t = 47, 107, 153, 221$  min), reaching the reconnection site and affecting the CBP dynamics as well as its brightness. Such features could be the result of the interaction of chromospheric waves and shocks with the CBP magnetic structure. A detailed analysis will be covered in a follow-up paper.

Rapid upflows can be seen associated with the CBP all along the experiment, as visualized through the blue-purple volume rendering in panel (a), which show velocities from 45 to 75 km s<sup>-1</sup>, and through the vertical velocity  $u_z$  in panel (e). These upflows are mainly concentrated around the spines of the CBP; those along the outer spine are basically reconnection outflows emanating from the nullpoint, whereas the ones around the inner spine are probably due to channeling of magnetosonic waves. The flows arising from the CBP nullpoint, like the one at the time of the figure, are of particular interest for the corona. These hot (1–2 MK) collimated ejections have low contrast in density compared to the surrounding plasma, and therefore they are not (or barely) distinguishable in the synthetic EUV images (see discussion in Section 3).

### 2.2. Energization

To address the fundamental question about the sustained CBP heating and its location, we have first analyzed the heating per unit mass due to the Joule and viscous terms. Panels (a) and (b) of Figure 2 contain time-averaged results over approximately 4.5 hours of the simulation at three different

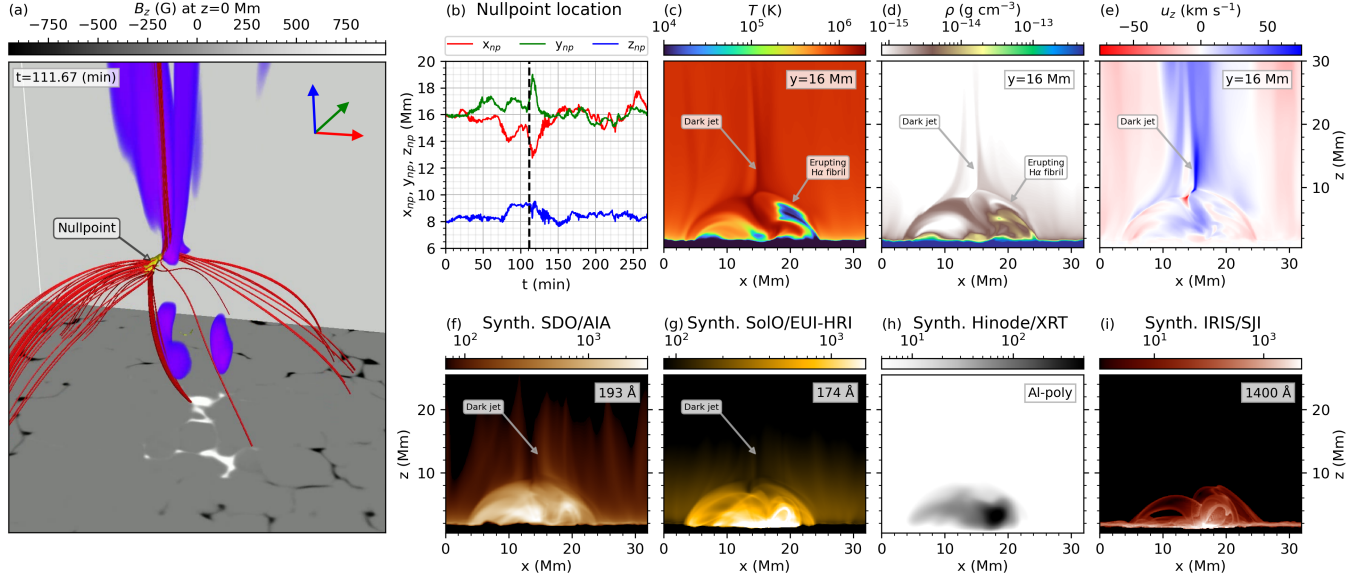


**Figure 1.** Experiment overview. (a) 3D magnetic nullpoint topology (red lines) at  $t = 111.67$  min superimposed on a horizontal map of  $B_z$  at  $z = 0$ . Blue-purple volume rendering corresponds to upflows with velocities from 45-75  $\text{km s}^{-1}$ . The yellow isosurface at  $B = 1$  G harbors the nullpoint location at the center of the image. The red-green-blue coordinate system indicates the  $x$ - $y$ - $z$  axis orientation. (b) Time-evolution of the nullpoint location coordinates ( $x_{np}$ ,  $y_{np}$ ,  $z_{np}$ ). (c), (d), (e) Temperature, density, and vertical velocity cuts at  $y = 16$  Mm, respectively. (f), (g), (h), (i) Synthetic response integrated along the  $y$ -axis to mimic a limb observation by SDO/AIA 193 Å, SoLo/EUI-HRI 174 Å, Hinode/XRT Al-poly (reversed color scale), and IRIS/SJI 1400 Å, respectively, in  $\text{DN s}^{-1} \text{pix}^{-1}$  units. The associated animation comprises the whole experiment evolution from  $t = 0$  to  $t = 268.33$  min.

(An animation of this figure is available.)

heights,  $z = [8, 5, 2]$  Mm, thus encompassing the regions in close proximity to the CBP nullpoint downwards to the low atmosphere. Both the Joule heating (left column) and viscous heating (right column) primarily occur at lower heights, at a few megameters above the solar surface, concentrated around the inner spine, in the region dominated by the strong parasitic positive polarity. We found that in these regions the electric current vector subtends a small angle with respect to the concentrated nearly vertical magnetic field, indicating that the magnetic configuration is close to force-free there. Heating is also found, albeit to a lesser extent, in the magnetic patches outside of the fan surface in the surroundings of the CBP at  $z = 2$  Mm (bottom panels), as well as in the region near the nullpoint at  $z = 8$  Mm (top panels). Thus, our findings indicate that CBP loops are primarily heated in the low atmosphere, with a secondary contribution at coronal heights near the reconnection site. Furthermore, there is a remarkable spatial correlation between the Joule and viscous heating across various heights. This suggests that regions exhibiting the highest electric current intensity and velocity gradient typically coincide. As a consequence, our results concerning the location of the CBP heating could be general, regardless of which mechanism (Joule or viscous) is dominant, even if in our experiment the Joule heating term is approximately one order of magnitude greater than the viscous one (see discussion in Section 3).

Another important question for CBPs, and for the corona in general, concerns whether the heating occurs on short or

long timescales (Reale 2014). To pursue this question, panels (c) and (d) of Figure 2 illustrate, as a function of time, the horizontal average within the CBP fan surface of the Joule (black) and viscous (orange) heating per unit mass at  $z = [2, 5]$  Mm, respectively. Both heating mechanisms seem to be continuously at work, showing fluctuations with different time scales. For instance, the pronounced peak observed mainly in the viscous heating profile at  $z = 5$  Mm at  $t \in [110, 120]$  min corresponds to the  $H\alpha$  fibril eruption explained in the previous section. In general, there is a clear time correlation between the Joule and viscous dissipation mechanisms. In fact, the Pearson correlation coefficient  $r$  between them is greater than 0.8 for the different heights we have analyzed.

As a final point, we consider the energy injection through the Poynting flux. Panel (e) of Figure 2 contains the mean vertical Poynting flux computed within the CBP fan surface and averaged in time,  $\langle S_z \rangle$ , as a function of height (blue curve). This plot strongly suggests that the heating of the plasma within the CBP domain is due to the deposition of the upward Poynting flux, which, itself, results from the stochastic photospheric motions stressing the CBP magnetic field. This implies that no major organized photospheric flows (leading, e.g., to spine dragging or convergence of magnetic polarities) are necessary to maintain the heating of the CBPs. Importantly, the average  $\langle S_z \rangle$  within the CBP is larger at all the heights than the corresponding quantity in the surroundings (red curve), and the same applies to the cor-

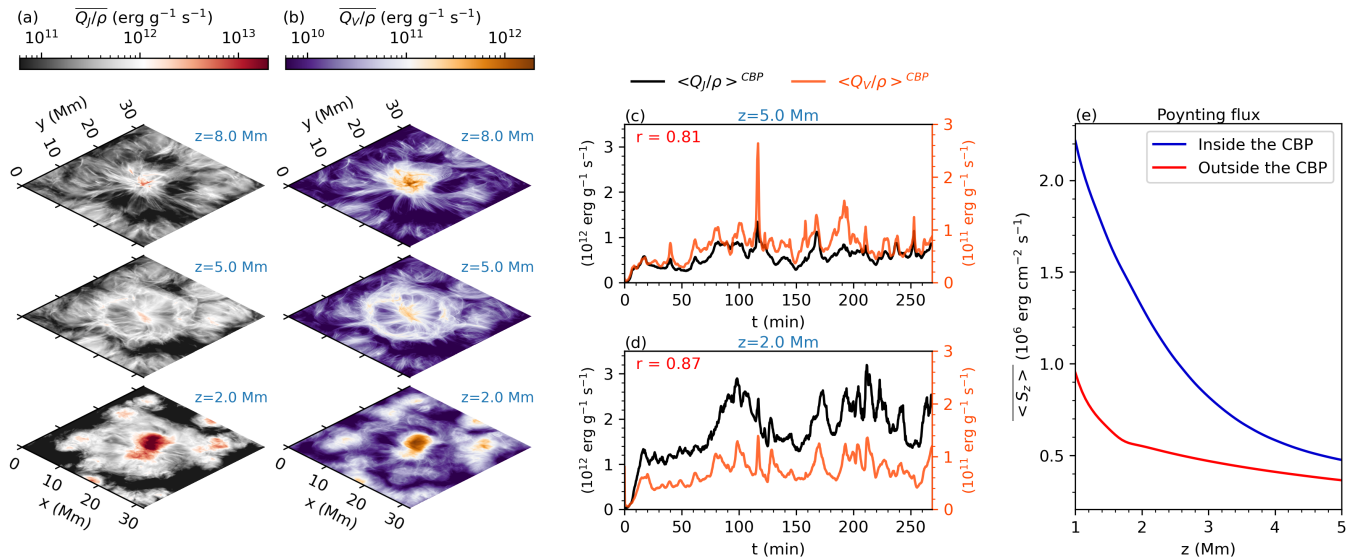


**Figure 2.** Heating in our CBP model. (a), (b) Heating per unit mass averaged over  $\sim 4.5$  hours for the Joule ( $\overline{Q_J/\rho}$ ) and viscous ( $\overline{Q_V/\rho}$ ) terms, respectively, at  $z = [8, 5, 2]$  Mm. (c), (d) Heating per unit mass averaged horizontally within the CBP at  $z = [5, 2]$  Mm, respectively, for the Joule ( $\langle Q_J/\rho \rangle^{CBP}$ , black) and viscous ( $\langle Q_V/\rho \rangle^{CBP}$ , orange) terms as a function of time. The Pearson correlation coefficient  $r$  between the curves is shown in red in the upper left corner of the plot frame. (e) Time average of the horizontal mean vertical Poynting flux ( $\langle S_z \rangle$ ) within the CBP (blue) and in the coronal hole surroundings (red).

responding gradient in height (in absolute value). The greater vertical Poynting flux obtained within the CBP is due to the strong magnetic concentration in the parasitic polarity. The Poynting flux values and the height gradient are in agreement with those indicated by other radiative-MHD numerical experiments as necessary to sustain heating in the quiet Sun corona (Rempel 2017; Chen et al. 2022). In addition, these values seem to fulfill the energy requirements for a hot corona inferred from observations (e.g.,  $0.8 \times 10^6$  erg cm $^{-2}$  s $^{-1}$  for coronal holes, Withbroe & Noyes 1977). Moreover, computing the surface integral of the vertical Poynting flux within the fan surface domain over two horizontal planes in the corona (e.g.,  $z = 2$  Mm and  $z = 5$  Mm), we obtain a magnetic energy deposition in the CBP of  $\approx 7 \times 10^{24}$  erg s $^{-1}$ , which is more than enough to explain the rough estimate of the CBP energy losses obtained through observations ( $10^{23}$  to  $10^{24}$  erg s $^{-1}$ , Habbal & Withbroe 1981). The loss of electromagnetic energy through the fan surface is most probably small by comparison, at any rate when averaging in time.

### 2.3. Confronting Observations and Modeling

To reinforce the previous results, we present here SDO and SST observations (see Appendix B) of a CBP that occurred on 2022 July 01 located at heliocentric coordinates  $(x, y) = (177'', 147'')$ . The million-K coronal response of the CBP, shown in the SDO/AIA images (panels (a) and (b) of Figure 3), has a compact and bright rowel-like shape that covers a horizontal domain of  $\sim 40'' \times 40''$ . The photospheric line-of-sight magnetic field image from SST/CRISP in panel (d) shows a parasitic negative polarity at the center of the CBP, surrounded by a dominant opposite polarity magnetic region, a configuration that can naturally lead to

a fan-spine configuration with a nullpoint at coronal heights (Zhang et al. 2012; Mou et al. 2016; Galsgaard et al. 2017; Madjarska et al. 2021; Cheng et al. 2023). The chromospheric H $\alpha$  core image from SST/CRISP in panel (c) indicates that the CBP contains a bunch of dark and long H $\alpha$  fibrils that connect opposite polarities, analogous to fibrils reported in lower resolution observations (Madjarska et al. 2021); and there are strong brightenings mainly located at the base of the fibrils, possibly indicative of chromospheric heating. The spectral profiles at different locations of the fibrils and brightenings are shown in panel (e).

In order to prove that our model satisfactorily reproduces the observations, Figure 4 and its associated animation contain the forward-modeling results from the simulations. Panel (a) shows that we indeed obtain a rowel-like structure composed of hot loops with enhanced EUV response similar to the SDO/AIA 193 Å observations, although our CBP is smaller than the observed one. Given its current interest, in panel (b) we also add the EUV response as would be observed by Solar Orbiter’s EUI instrument, with its higher spatial resolution. The comparison to observations is also successful for the chromospheric counterpart, as seen in panel (c). Our CBP model is realistic enough to reproduce a pattern of elongated dark fibrils, as observed in the H $\alpha$  images; and the existence of strong brightenings at the base of these fibrils, surely a manifestation of the location of the heating in the lower atmosphere, as discussed in the previous section. The agreement is further illustrated by comparing panels (e) of Figures 3 and 4. The observational and synthetic spectral profiles show a similar behaviour regarding the H $\alpha$  line core intensity at different locations of the fibrils and brightenings, namely, the fibrils are character-

ized by a less bright  $H\alpha$  core than the average with a small Doppler shift, while the brightenings show an enhanced  $H\alpha$  core. The smaller width in the synthetic profiles may be due to the modest numerical resolution not capturing the highly dynamic complexity of the chromosphere (Hansteen et al. 2023). At the photosphere, the vertical magnetic field of the model (panel (d) of Figure 4) shows that the elongated  $H\alpha$  fibrils connect the central parasitic polarity with the strong, opposite-polarity magnetic patches surrounding the CBP, as shown in our observations (panel (d) of Figure 3) as well as in other CBP observations (Madjarska et al. 2021).

### 3. DISCUSSION

In this Letter, through a 3D radiative-MHD model using the Bifrost code, we have shown that CBPs can be energized by the action of the continuous surface convection motions, thus obviating the need for major, organized photospheric flows such as converging flows (Priest et al. 1994; Dreher et al. 1997; Priest et al. 2018; Syntelis et al. 2019) or large-scale surface flows (Wyper et al. 2018). Our investigation reveals that the CBP loops are heated by both Joule and viscous heating predominantly in the lower atmosphere, with a secondary contribution at coronal heights close to the reconnection site. This is a major difference with 2D models (e.g., Syntelis et al. 2019; Nóbrega-Siverio & Moreno-Insertis 2022), which can only capture the heating at the reconnection site since mechanisms, such as magnetic field-line braiding, are intrinsically three-dimensional. The heating rate from both the resistive and viscous heating terms is intermittent, which seems to be consistent with findings from simulations focused on individual coronal loops (Breu et al. 2022). Furthermore, both the spatial and time correlation found between the Joule and viscous heating within the CBP suggests that the heating results obtained in this Letter may be widely independent of the value of the magnetic Prandtl number, in line with the conclusions reached in recent coronal numerical simulations (Rempel 2017; Chen et al. 2022). This implies that, even though current numerical models are far from reproducing the Prandtl numbers of the solar atmosphere, our results may well be applicable to understand the heating of small-scale loops (CBPs) and their properties.

By means of X-ray, EUV, and UV forward modeling, we have shown that the CBP’s multi-wavelength response and corresponding brightness exhibit fluctuations on the scale of minutes (see animation of Figure 1), resembling intensity variations reported in observations (Ugarte-Urra et al. 2004; Doschek et al. 2010; Kumar et al. 2011; Ning & Guo 2014; Zhang et al. 2014; Chandrashekhar & Sarkar 2015; Kayshap & Dwivedi 2017; Gao et al. 2022). Our results also indicate that chromospheric phenomena, such as  $H\alpha$  fibrils and spicule-like features, can perturb the CBP, leading to significant changes in the EUV intensity. These findings support the recent results about the impact of spicules in the CBP brightness variations (Nóbrega-Siverio & Moreno-Insertis 2022; Bose et al. 2023). Additionally, our model demonstrates that CBPs can produce collimated hot ejections that do not show appreciable emission in EUV due to the slight density

contrast with the surroundings. This may offer theoretical support to the observed features rooted in CBPs named *dark jets* that have been detected in EUV spectroscopic data using Hinode/EIS, but with either weak or absent signatures in SDO/AIA 193 Å images (Young 2015). This may be also the key to explaining the lack of clear observable jetting activity in EUV images in the early stages of CBPs (Kumar et al. 2019). Further observational evidence using off-limb examples and spectroscopic observations is needed. In this vein, our results could provide valuable insights for the near future missions Multi-slit Solar Explorer (MUSE, De Pontieu et al. 2022; Cheung et al. 2022) and Solar-C/EUVST (Shimizu et al. 2020).

In this Letter, we have also provided simultaneous observations of a representative CBP from SDO and SST. Thus, we not only address the scarcity of observational results about the chromosphere below CBPs (Madjarska et al. 2021; Bose et al. 2023), but also we impose a case-study to test our model. The similarities between the synthetic observables from the model and the observations are striking, even reproducing chromospheric features such as the brightenings in the core of the  $H\alpha$  line, the dark and elongated  $H\alpha$  fibrils, as well as their magnetic photospheric connections. By increasing the numerical resolution, we expect to achieve even greater agreement with the observations in aspects such as the width of the  $H\alpha$  line and the intricate fine structure within CBPs. All the results described above are a good indication that we are including the most important physical ingredients to explain the evolution and heating of CBPs as well as reproducing their main identifying signatures.

This research has been supported by the European Research Council through the Synergy Grant number 810218 (“The Whole Sun”, ERC-2018-SyG); by the Spanish Ministry of Science, Innovation and Universities through project PGC2018-095832-B-I00; and by the Research Council of Norway (RCN) through its Centres of Excellence scheme, project number 262622. The authors acknowledge the computer resources at the MareNostrum supercomputing installation and the technical support provided by the Barcelona Supercomputing Center (BSC, RES-AECT-2021-1-0023, RES-AECT-2022-2-0002). The use of UCAR’s VAPOR software (Li et al. 2019; Pearse et al. 2023) is gratefully acknowledged. This work also benefited from discussions at the International Space Science Institute (ISSI) in Bern, through ISSI International Team project #535 *Unraveling surges: a joint perspective from numerical models, observations, and machine learning*. L.R.v.d.V. is supported by RCN project number 325491. M.M. acknowledges financial support by DFG grant WI 3211/8-1. The Swedish 1-m Solar Telescope is operated on the island of La Palma by the Institute for Solar Physics of Stockholm University in the Spanish Observatorio del Roque de Los Muchachos of the Instituto de Astrofísica de Canarias. The Institute for Solar Physics is supported by a grant for research infrastructures of national importance from the Swedish Research Council (registration number 2017-00625). SDO observations are courtesy of NASA/SDO and

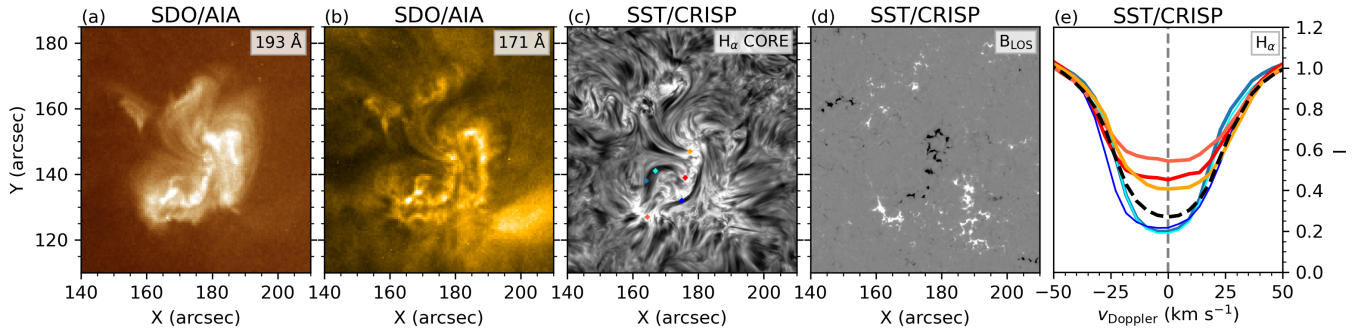


**Figure 3.** Observations of a representative CBP on 2022 July 01 at 08:08:52 UT. (a), (b) Hot coronal response in EUV detected by SDO/AIA 193 Å and SDO/AIA 171 Å, respectively. (c) Cool chromospheric structure of the CBP in the H $\alpha$  line core observed with SST/CRISP. (d) Photospheric line-of-sight (LOS) magnetic field ( $B_{\text{LOS}}$ ) from SST/CRISP. (e) H $\alpha$  profiles for different regions of the dark fibrils (cool colors) and core brightenings (warm colors) marked in panel (c). The average profile over the whole field-of-view is shown as a black dashed line. The intensity of the profiles has been normalized to the intensity value at  $50 \text{ km s}^{-1}$ .

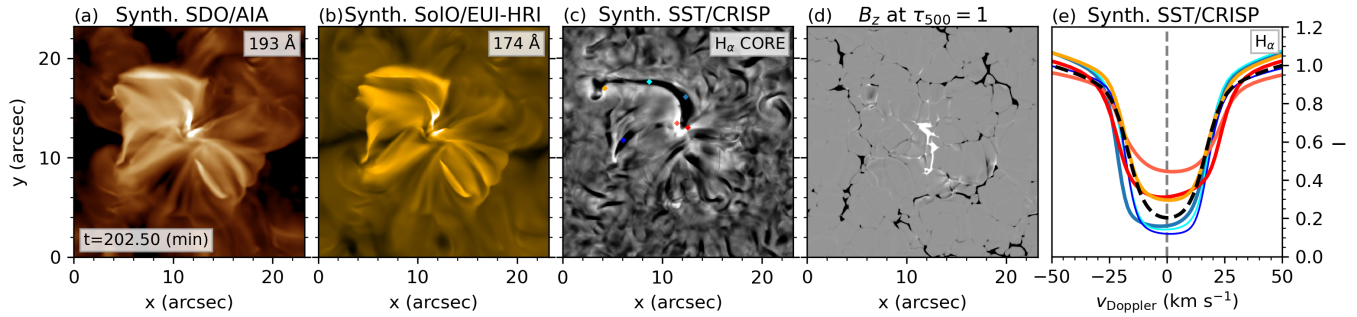


**Figure 4.** Forward modeling from our 3D CBP numerical experiment as observed on-disk. (a), (b) Synthetic EUV images for SDO/AIA 193 Å and SoLO/EUI-HRI 174 Å, respectively. (c) Synthetic H $\alpha$  response in the core of the line as observed by SST/CRISP. (d) Vertical magnetic field  $B_z$  at the solar surface ( $\tau_{500 \text{ nm}} = 1$ ). (e) H $\alpha$  profiles for different regions of the dark fibrils (cool colors) and core brightenings (warm colors) marked in panel (c). The average profile over the whole box is shown as a black dashed line. The intensity of the profiles has been normalized to the intensity value at  $50 \text{ km s}^{-1}$ . The associated animation shows the synthetic results for  $t = 111.67, 202.50, \text{ and } 264.17 \text{ min}$ . (An animation of this figure is available.)

the AIA, EVE, and HMI science teams. The authors thank

Dr. Frédéric Auchère for his help to compute the synthetic observables for SoLO/EUI-HRI.

## APPENDIX

### A. NUMERICAL EXPERIMENT

#### A.1. Code

The experiment was carried out using the radiation-magnetohydrodynamics Bifrost code (Gudiksen et al. 2011). This code includes, in a self-consistent manner, radiative transfer from the photosphere to the corona; approximate recipes for the main radiative losses in the chromosphere due to neutral hydrogen, singly-ionized calcium, and singly-ionized magnesium; field aligned thermal conduction, which tends to an isotropic conductivity prescription for regions with weak magnetic field such as nullpoints; optically thin losses; and an equation of state considering the 16 most relevant atomic elements for the solar atmosphere either because of their high abundance or because of their importance

as electron donors at low temperatures. Explicit resistivity and viscosity are included in Bifrost through hyper-diffusion terms (Gudiksen et al. 2011), following the idea originally described by Nordlund & Galsgaard (1995). A comprehensive description of the resistive and viscous hyper-diffusion operator and the associated free parameters can be found in the papers by Færder et al. (2023a,b), including a comparative analysis of the hyper-diffusive resistivity versus other resistivity models.

#### A.2. Initial Condition

The initial condition was built using a weakly magnetized (0.2 G at the corona) preexisting 3D numerical experiment that had reached a statistically stationary equilibrium. In the

vertical direction, the numerical box covers a region from the uppermost layers of the solar interior to the corona, that is,  $-2.9 \text{ Mm} \leq z \leq 32.3 \text{ Mm}$ , with  $z = 0$  corresponding to the solar surface (more precisely the horizontal surface where  $\langle \tau_{500 \text{ nm}} \rangle = 1$ ). The horizontal extent is  $32 \times 32.0 \text{ Mm}^2$ , with both  $x$  and  $y$  starting at the origin of coordinates  $(0, 0)$ . The domain is resolved with  $512 \times 512 \times 512$  cells, employing a uniform grid in the horizontal directions with spacing  $\Delta x = \Delta y = 62.5 \text{ km}$ ; and a non-uniform mesh for  $z$ , using  $\Delta z = 50 \text{ km}$  from the interior up to  $12 \text{ Mm}$  in the corona, and then progressively decreasing the resolution down to  $\Delta z = 150 \text{ km}$  at the top of the corona. The boundary conditions are periodic in the horizontal direction. In the vertical direction, at the top, characteristic boundary conditions are applied; at the bottom, constant entropy is set for the incoming plasma to keep solar-like convection, while the rest of the variables are extrapolated. Panel (a) of Figure A1 shows the horizontal averages of the temperature  $T$  and mass density  $\rho$  of the background stratification.

On top of the relaxed snapshot mentioned above, we added a potential magnetic nullpoint distribution as illustrated in panel (b) of Figure A1. The potential configuration was calculated from a prescribed axisymmetric distribution at the bottom boundary containing a circular positive polarity (the *parasitic* polarity) embedded in a negative background. This imposed configuration is such that (a) there is a nullpoint at  $(x_{np}, y_{np}, z_{np}) = (16, 16, 8) \text{ Mm}$ ; (b) at large heights, the magnetic field becomes asymptotically vertical and uniform with  $B_z \rightarrow -10 \text{ G}$ , thus mimicking a coronal hole structure; and (c) at  $z = 0$ , the total positive flux is  $\Phi^+ = 4.9 \times 10^{19} \text{ Mx}$ , the maximum positive vertical field strength is  $B_z = 141.8 \text{ G}$ , the parasitic polarity covers a circular patch of radius  $6.3 \text{ Mm}$ , and the intersection of the fan surface with the horizontal plane has a radius of  $12.4 \text{ Mm}$ .

## B. OBSERVATIONS

### B.1. The Swedish 1-m Solar Telescope (SST) Data.

We have used observations from the SST (Scharmer et al. 2003) obtained on 2022 July 01 from 08:04:57 to 08:13:03 UT centered at a CBP located at heliocentric coordinates  $(x, y) = (176'', 135'')$ . To cover the whole CBP and surroundings within the field-of-view (FOV) of the SST instrumentation, we have created a mosaic constructed from  $3 \times 3$  telescope pointings. The SST data set contains the following spectral scans from the CRISP Imaging Spectropolarimeter (CRISP, Scharmer et al. 2008): the Fe I 6173 Å line in spectropolarimetric mode sampled in 14 positions between  $-320 \text{ mÅ}$  and  $+680 \text{ mÅ}$  from the line core, and H $\alpha$  6563 Å in spectroscopic mode sampled in 31 positions ranging from  $-1500 \text{ mÅ}$  to  $+1500 \text{ mÅ}$  from the line core. Each of the CRISP scans of the mosaic has a FOV of  $\sim 58'' \times 58''$  and a spatial sampling of  $0''.057$  per pixel. The CRISP data were processed using the SSTRED data reduction pipeline (de la Cruz Rodríguez et al. 2015; Löfdahl et al. 2021), which includes Multi-Object Multi-Frame Blind Deconvolution (MOMFBD, van Noort et al. 2005) image restoration. Line-of-sight (LOS) magnetograms were obtained by Milne-

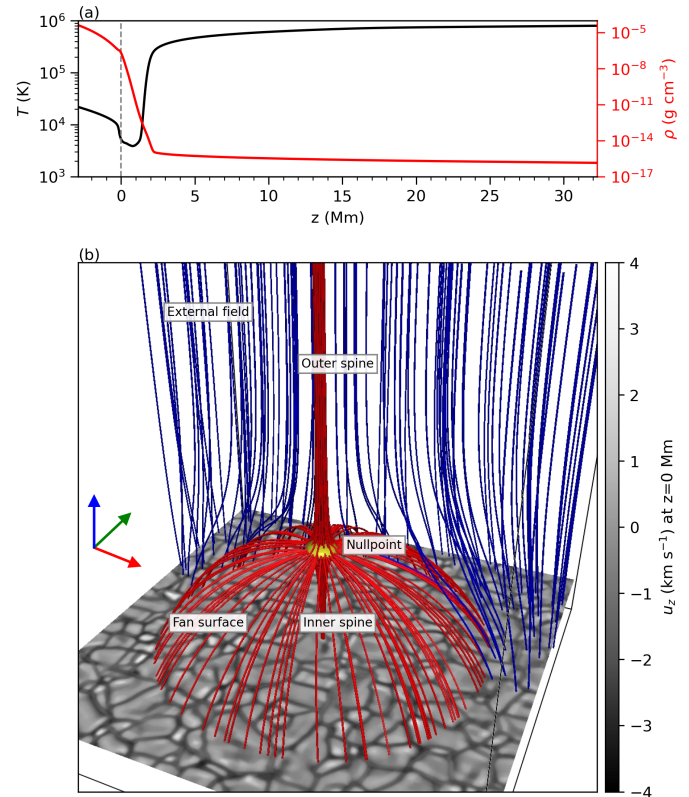


**Figure A1.** Initial condition. (a) Initial horizontal average stratification for the temperature  $T$  and density  $\rho$ . (b) Imposed nullpoint magnetic field configuration (red lines) embedded within a coronal-hole like magnetic field (blue). The yellow isosurface at  $B = 1 \text{ G}$  delimits the nullpoint location. Other features of this configuration are also highlighted following the 3D nullpoint terminology (Priest & Titov 1996). The solar granulation pattern of the initial model is shown through the vertical velocity  $u_z$  at  $z = 0$ . The red-green-blue coordinate system indicates the orientation of the x-y-z axis.

Eddington inversions of the Fe I 6173 Å Stokes profiles (de la Cruz Rodríguez 2019).

### B.2. The Solar Dynamics Observatory (SDO) Data.

The coronal response of the targeted CBP is obtained from the Atmospheric Imaging Assembly (AIA, Lemen et al. 2012) onboard SDO (Pesnell et al. 2012) around 08:08:52 UT: the time at which the center of the SST mosaic was taken. The photospheric magnetic field is obtained from the Helioseismic and Magnetic Imager (HMI, Scherrer et al. 2012). Regarding the alignment, cross-alignment is carried out in all the AIA channels to the HMI continuum; then, the SDO images are manually aligned with the SST ones.

## C. FORWARD MODELING

### C.1. EUV and UV Forward Modeling.

For the forward modeling in the EUV and UV, the expressions of optically thin radiative transfer are used, assuming,

additionally, coronal abundances (Feldman 1992) and ionization equilibrium. The emissivity corresponding to any given transition between electron configuration levels  $i$  and  $j$  of a given ionic species of an atomic element (e.g., Fe IX, or Si IV) is given by

$$\epsilon = n_H n_e G(T, n_e, \nu_{ij}) \quad (\text{C1})$$

where  $n_e$  and  $n_H$  are the electron and hydrogen number densities, respectively;  $\nu_{ij}$  is the radiation frequency of the emitted photon; and  $G(T, n_e, \nu_{ij})$  is the corresponding gain function (or contribution function), which already contains the abundance of the atomic element. The emitted intensity is calculated by integrating Equation C1 along the LOS in the numerical box.

For the SDO/AIA coronal synthetic images, we have used CHIANTI (Del Zanna et al. 2021) from the Solar Soft package, calculating the gain functions for the atomic transitions in the relevant spectral range of the different AIA filters and weighing with the corresponding effective Area Function. The result is then transformed into SDO/AIA count numbers. To account for the possible obscuration effects from cool and dense features in the EUV images, we have included absorption by neutral hydrogen, neutral helium, and singly-ionized helium in the integration of the emissivity along the LOS adding an absorption factor  $e^{-\tau}$  following the recipes and procedures in the literature (De Pontieu et al. 2009; Anzer & Heinzel 2005).

For the synthetic 174 Å images of the Extreme Ultraviolet Imager of the High Resolution Imager (EUI-HRI) (Rochus et al. 2020); on Solar Orbiter (SoLO) (Müller et al. 2020), we have employed a contribution function privately provided by Dr. Frédéric Auchère, member of the Solar Orbiter team.

For the synthetic IRIS (De Pontieu et al. 2014) transition region counterpart, the contribution function of the Si IV 1393.755 Å line is obtained through a simple procedure (Chi-anti Solar Soft routine `ch_synthetic.pro` with the flag `/gofit`), multiplying the output by the silicon abundance

relative to hydrogen. This procedure and the conversion to IRIS count numbers are detailed in a recent paper (Nóbrega-Siverio et al. 2017).

After obtaining the intensity images, we have degraded the results to match the spatial resolution of the instruments, namely, 1''5 for SDO/AIA (Lemen et al. 2012); 0''33 for IRIS (De Pontieu et al. 2014); and 200 km for EUI-HRI at perihelion (Rochus et al. 2020).

### C.2. X-ray Forward Modeling.

The X-ray synthetic images have been computed to mimic observations taken by the X-ray telescope (XRT) (Golub et al. 2007) onboard Hinode (Kosugi et al. 2007). In particular, we have combined the `make_xrt_wave_resp.pro` and `make_xrt_temp_resp.pro` routines from Solar Soft to obtain the spectral and temperature response for the Al-poly channel of the telescope. The result is correspondingly multiplied by the squared electron number density and then degraded to the 2''0 instrument resolution (Golub et al. 2007).

### C.3. Chromospheric Forward Modeling.

To obtain H $\alpha$  synthetic images, we have used the 3D non-LTE radiative transfer code Multi3D (Leenaarts & Carlsson 2009). Multi3D evaluates the radiation field in full 3D taking the horizontal structure of 3D model atmospheres into account. To reduce the 3D radiative transfer computation cost, we have halved the horizontal resolution of the model atmosphere. We further optimized the depth scaling of the atmospheric quantities to improve the convergence time and to reduce the effect of an insufficiently sampled optical depth scale onto the synthesized H $\alpha$  line profiles. H $\alpha$  was synthesized from a five-level plus continuum hydrogen model atom assuming Doppler line profiles for the Ly $\alpha$  and Ly $\beta$  lines which affect the level populations of the H $\alpha$  transition (Leenaarts et al. 2012). We have reduced the spatial resolution of the synthetic images to the SST/CRISP instrumental values, namely, 0.''13 at 6301 Å (Scharmer et al. 2008).

## REFERENCES

- Anzer, U., & Heinzel, P. 2005, *ApJ*, 622, 714
- Bose, S., Nóbrega-Siverio, D., De Pontieu, B., & Rouppe van der Voort, L. 2023, *ApJ*, 944, 171
- Breu, C., Peter, H., Cameron, R., et al. 2022, *A&A*, 658, A45
- Chandrasekhar, K., & Sarkar, A. 2015, *ApJ*, 810, 163
- Chen, F., Rempel, M., & Fan, Y. 2022, *ApJ*, 937, 91
- Cheng, X., Priest, E. R., Li, H. T., et al. 2023, *Nature Communications*, 14, 2107
- Cheung, M. C. M., Martínez-Sykora, J., Testa, P., et al. 2022, *ApJ*, 926, 53
- de la Cruz Rodríguez, J. 2019, *A&A*, 631, A153
- de la Cruz Rodríguez, J., Löfdahl, M. G., Sütterlin, P., Hillberg, T., & Rouppe van der Voort, L. 2015, *A&A*, 573, A40
- De Pontieu, B., Hansteen, V. H., McIntosh, S. W., & Patsourakos, S. 2009, *ApJ*, 702, 1016
- De Pontieu, B., Title, A. M., Lemen, J. R., et al. 2014, *SoPh*, 289, 2733
- De Pontieu, B., Testa, P., Martínez-Sykora, J., et al. 2022, *ApJ*, 926, 52
- Del Zanna, G., Dere, K. P., Young, P. R., & Landi, E. 2021, *ApJ*, 909, 38
- Doschek, G. A., Landi, E., Warren, H. P., & Harra, L. K. 2010, *ApJ*, 710, 1806
- Dreher, J., Birk, G. T., & Neukirch, T. 1997, *A&A*, 323, 593
- Færder, Ø. H., Nóbrega-Siverio, D., & Carlsson, M. 2023a, *A&A*, 675, A97
- . 2023b, *submmited*



- Feldman, U. 1992, *PhyS*, 46, 202
- Galsgaard, K., Madjarska, M. S., Moreno-Insertis, F., Huang, Z., & Wiegmann, T. 2017, *A&A*, 606, A46
- Galsgaard, K., & Nordlund, Å. 1996, *J. Geophys. Res.*, 101, 13445
- Galsgaard, K., Parnell, C. E., & Blaizot, J. 2000, *A&A*, 362, 395
- Gao, Y., Tian, H., Van Doorselaere, T., & Chen, Y. 2022, *ApJ*, 930, 55
- Golub, L., Krieger, A. S., Silk, J. K., Timothy, A. F., & Vaiana, G. S. 1974, *ApJL*, 189, L93
- Golub, L., Deluca, E., Austin, G., et al. 2007, *SoPh*, 243, 63
- Gudiksen, B. V., Carlsson, M., Hansteen, V. H., et al. 2011, *A&A*, 531, A154
- Gudiksen, B. V., & Nordlund, Å. 2005, *ApJ*, 618, 1020
- Habbal, S. R., & Withbroe, G. L. 1981, *SoPh*, 69, 77
- Hansteen, V. H., Martinez-Sykora, J., Carlsson, M., et al. 2023, *ApJ*, 944, 131
- Hong, J., Jiang, Y., Yang, J., et al. 2014, *ApJ*, 796, 73
- Javadi, S., Büchner, J., Otto, A., & Santos, J. C. 2011, *A&A*, 529, A114
- Kayshap, P., & Dwivedi, B. N. 2017, *SoPh*, 292, 108
- Klimchuk, J. A. 2006, *SoPh*, 234, 41
- Kosugi, T., Matsuzaki, K., Sakao, T., et al. 2007, *SoPh*, 243, 3
- Kumar, M., Srivastava, A. K., & Dwivedi, B. N. 2011, *MNRAS*, 415, 1419
- Kumar, P., Karpen, J. T., Antiochos, S. K., et al. 2019, *ApJ*, 873, 93
- Leenaarts, J., & Carlsson, M. 2009, in *Astronomical Society of the Pacific Conference Series*, Vol. 415, *The Second Hinode Science Meeting: Beyond Discovery-Toward Understanding*, 87
- Leenaarts, J., Carlsson, M., & Rouppe van der Voort, L. 2012, *ApJ*, 749, 136
- Lemen, J. R., Title, A. M., Akin, D. J., et al. 2012, *SoPh*, 275, 17
- Li, S., Jaroszynski, S., Pearse, S., Orf, L., & Clyne, J. 2019, *Atmosphere*, 10, 488
- Lionello, R., Török, T., Titov, V. S., et al. 2016, *ApJL*, 831, L2
- Löfdahl, M. G., Hillberg, T., de la Cruz Rodríguez, J., et al. 2021, *A&A*, 653, A68
- Madjarska, M. S. 2019, *Living Reviews in Solar Physics*, 16, 2
- Madjarska, M. S., Chae, J., Moreno-Insertis, F., et al. 2021, *A&A*, 646, A107
- Madjarska, M. S., Mackay, D. H., Galsgaard, K., Wiegmann, T., & Xie, H. 2022, *A&A*, 660, A45
- Mondal, B., Klimchuk, J. A., Vadawale, S. V., et al. 2023, *ApJ*, 945, 37
- Mou, C., Huang, Z., Xia, L., et al. 2016, *ApJ*, 818, 9
- Müller, D., St. Cyr, O. C., Zouganelis, I., et al. 2020, *A&A*, 642, A1
- Ning, Z., & Guo, Y. 2014, *ApJ*, 794, 79
- Nóbrega-Siverio, D., Martínez-Sykora, J., Moreno-Insertis, F., & Rouppe van der Voort, L. 2017, *ApJ*, 850, 153
- Nóbrega-Siverio, D., & Moreno-Insertis, F. 2022, *ApJL*, 935, L21
- Nordlund, Å., & Galsgaard, K. 1995, *A 3D MHD Code for Parallel Computers*
- Parker, E. N. 1972, *ApJ*, 174, 499
- Parnell, C. E., & De Moortel, I. 2012, *Philosophical Transactions of the Royal Society of London Series A*, 370, 3217
- Pearse, S., Li, S., Clyne, et al. 2023, *NCAR/VAPOR: Vapor 3.8.1, 3.8.1*, Zenodo
- Pesnell, W. D., Thompson, B. J., & Chamberlin, P. C. 2012, *SoPh*, 275, 3
- Priest, E. R., Chitta, L. P., & Syntelis, P. 2018, *ApJL*, 862, L24
- Priest, E. R., Parnell, C. E., & Martin, S. F. 1994, *ApJ*, 427, 459
- Priest, E. R., & Titov, V. S. 1996, *Philosophical Transactions of the Royal Society of London Series A*, 354, 2951
- Rappazzo, A. F., Velli, M., Einaudi, G., & Dahlburg, R. B. 2008, *ApJ*, 677, 1348
- Reale, F. 2014, *Living Reviews in Solar Physics*, 11, 4
- Rempel, M. 2017, *ApJ*, 834, 10
- Rochus, P., Auchère, F., Berghmans, D., et al. 2020, *A&A*, 642, A8
- Santos, J. C., & Büchner, J. 2007, *Astrophysics and Space Sciences Transactions*, 3, 29
- Scharmer, G. B., Bjelksjö, K., Korhonen, T. K., Lindberg, B., & Petterson, B. 2003, in *Society of Photo-Optical Instrumentation Engineers (SPIE) Conference Series*, Vol. 4853, *Innovative Telescopes and Instrumentation for Solar Astrophysics*, ed. S. L. Keil & S. V. Avakyan, 341–350
- Scharmer, G. B., Narayan, G., Hillberg, T., et al. 2008, *ApJL*, 689, L69
- Scherrer, P. H., Schou, J., Bush, R. I., et al. 2012, *SoPh*, 275, 207
- Shimizu, T., Imada, S., Kawate, T., et al. 2020, in *SPIE Conference Series*, Vol. 11444, *Space Telescopes and Instrumentation 2020: Ultraviolet to Gamma Ray*, 114440N
- Sterling, A. C., Moore, R. L., Falconer, D. A., & Adams, M. 2015, *Nature*, 523, 437
- Syntelis, P., Priest, E. R., & Chitta, L. P. 2019, *ApJ*, 872, 32
- Ugarte-Urra, I., Doyle, J. G., Madjarska, M. S., & O'Shea, E. 2004, *A&A*, 418, 313
- van Noort, M., Rouppe van der Voort, L., & Löfdahl, M. G. 2005, *SoPh*, 228, 191
- Viall, N. M., & Borovsky, J. E. 2020, *Journal of Geophysical Research (Space Physics)*, 125, e26005
- von Rekowski, B., Parnell, C. E., & Priest, E. R. 2006, *MNRAS*, 366, 125
- Withbroe, G. L., & Noyes, R. W. 1977, *ARA&A*, 15, 363
- Wyper, P. F., DeVore, C. R., Karpen, J. T., Antiochos, S. K., & Yeates, A. R. 2018, *ApJ*, 864, 165
- Young, P. R. 2015, *ApJ*, 801, 124
- Zhang, Q. M., Chen, P. F., Ding, M. D., & Ji, H. S. 2014, *A&A*, 568, A30
- Zhang, Q. M., Chen, P. F., Guo, Y., Fang, C., & Ding, M. D. 2012, *ApJ*, 746, 19